RAPID COMMUNICATION

Gallium-arsenide deep-center laser

M. Gupta · J.L. Pan

Abstract In a novel approach to "thresholdless" lasers, we have developed a new growth technique for self-assembled deep centers in the technologically important semiconductor gallium-arsenide. Here we demonstrate the first gallium-arsenide deep-center laser. These lasers, which intentionally utilize gallium-arsenide deep-center transitions, exhibit a threshold of less than 2 A/cm^2 in continuous-wave mode at room temperature at the important 1.54 μm fiber-optic wavelength. This threshold is much lower than for bandgap transitions in conventional bulk semiconductors. It is significant that this first demonstration of broad-area laser action was accomplished with electrical injection, and not merely optical pumping, as is usual for a new material.

PACS 71.55.Eq · 71.55.-i · 78.67.-n · 81.10.-h · 85.60.Jb · 78.45.+h

1 Introduction

The ongoing quest for "thresholdless" [1] semiconductor lasers has led to the development of new materials (e.g., quantum wells [2], wires, and dots [3, 4]) and new optical resonators (e.g., microdisks [4] and photonic bandgap crystals [1]). In a novel effort towards "thresholdless" lasers, we recently demonstrated [5] that native deep-acceptor complexes in gallium-arsenide (GaAs) exhibited stimulated emission at very low current densities. Moreover, in contrast to conventional semiconductor devices, whose operating wavelengths are determined by the bandgap energy, we showed [5, 6] that the room-temperature stimulated emission from GaAs deep centers can be tuned very widely from the bandgap (∼900 nm) to half the bandgap (1600 nm). Here we demonstrate the first GaAs deep-center laser.

We recently [6] developed a growth technique which uses a high n-type doping to thermodynamically favor the formation of large concentrations of compensating deep-acceptors having energies below midgap. Though these deep-acceptors have been known since the 1960s [7–15], this material is novel because n-type GaAs is not usually designed to retain large concentrations of compensating acceptors. These compensating acceptors are [7, 8, 16–20] donor-vacancy-on-gallium complexes (donor-V_{Ga} complexes, e.g., V_{Ga}, Si_{Ga}–V_{Ga}, Si_{Ga}–V_{Ga}–Si_{Ga}, etc., where Si_{Ga} denotes the silicon-on-gallium-site). Figure 1 shows the relevant energy levels and measurement geometries. The conduction- and valence-band edges, the deep levels, and an upper state near the conduction band are denoted in Fig. 1a–b as, respectively, E_C, E_V, E_d, and E_U. Figure 1b shows the radiative transition between the state E_U near the conduction band and a deep state E_{d1}, as well as the fast capture [6] of free holes onto deep centers. The literature [7, 21, 22] says that the upper state E_U corresponds to a state centered on the donor in the donor-V_{Ga} complex, whereas the lower state E_d corresponds to a state centered on the V_{Ga} in the complex.

2 Methods

All samples were grown by molecular beam epitaxy on semiinsulating GaAs substrates. Sample A consisted of 3000 Å of undoped GaAs buffer, 1149 Å of AlAs etch stop,

M. Gupta · J.L. Pan (✉)
Yale University, P.O. Box 208284, New Haven, CT 06520-8284, USA
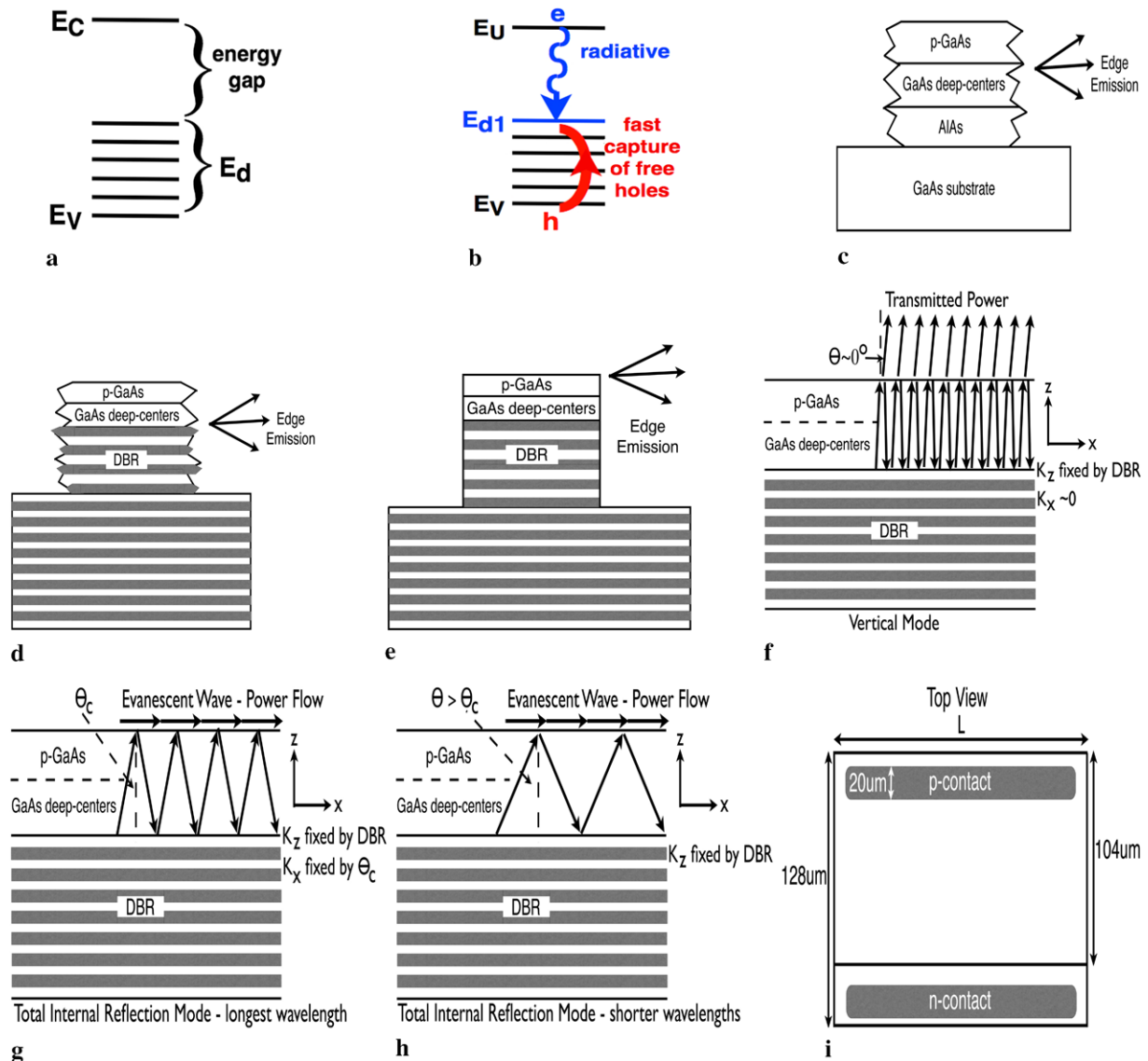e-mail: janet.pan@yale.edu
Fax: +1-203-432-6420

Fig. 1 (Color online) Energy levels and measurement geometries. **a** Deep levels in highly n-doped GaAs. **b** Radiative transition between a state E_U near the conduction band and a deep state E_{d1}. Free holes undergo fast capture onto deep centers. **c** Single-pass measurement from the edge of Sample A. The active layer was *not* placed within a resonant cavity or waveguide. **d** Single-pass measurement from the edge of Sample B. A bottom mirror (DBR) was added to increase the single-pass optical length. The rough wet-etched facets preclude the optical-feedback characteristic of resonant cavities. **e** Edge emission from Samples C–H. The RIE facets allow the formation of a resonant cavity, with its characteristic optical feedback. **f** "Vertical" waveguide mode, in which the longitudinal wave vector K_X is nearly zero. A lot of power is transmitted vertically through the top surface. **g** Longest wavelength total-internal-reflection mode. Here, rays from within the semiconductor are incident upon the sample surface at the critical angle θ_C for total-internal-reflection. **h** Shorter wavelength total-internal-reflection mode. Here, rays from within the semiconductor are incident upon the sample surface at an angle greater than θ_C. This mode makes fewer passes through the active region. **i** Top view of the semiconductor surface showing the pixel dimensions

2271 Å of GaAs deep centers, 399 Å of $Al_{0.45}Ga_{0.55}As$, above which was a 1294 Å GaAs layer p-doped at 3.2×10^{19} cm^{-3}. Sample B consisted of 3000 Å of undoped GaAs buffer, 42 periods of a distributed Bragg reflector (DBR, 1148 Å of GaAs and 1340 Å of AlAs), 2486 Å of GaAs deep centers, 399 Å of $Al_{0.45}Ga_{0.55}As$, above which was a 3143 Å GaAs layer p-doped at 3.2×10^{19} cm^{-3}. The growth which yielded Samples C–H consisted of 3000 Å of undoped GaAs buffer, 35 periods of a DBR (1104 Å of GaAs and 1266 Å of $Al_{0.86}Ga_{0.14}As$), 2108 Å of GaAs deep centers, 399 Å of $Al_{0.45}Ga_{0.55}As$, above which was a 1937 Å GaAs layer p-doped at 3.2×10^{19} cm^{-3}. The Si donor concentration in the deep-center layer was always 4.5–4.8×10^{19} cm^{-3}. We estimate that the concentration of Si_{Ga}–V_{Ga} in the deep-center layer was about ~ 1.5–2×10^{19} cm^{-3}. These samples were representative of several

dozen growths. Further details about the crystal growth were reported previously [6].

Devices were fabricated using standard photolithography, wet etches, and Ti–Au contacts. Pixels are shown in Fig. 1i. Individual devices were isolated from each other by etching 128 μm × L mesas in the n-type deep-center layer. Current was injected through 104 μm × L mesas in the p-type GaAs layer. In Samples A and B, L was 75 μm and 150 μm, respectively. The pixels in Samples A and B were fabricated with wet etches (phosphoric acid). The wet etches left the mesa edges with a random roughness. The isolation etch of Sample B extended 3.5 periods into the DBR. The pixels in Samples C–H were fabricated via reactive ion etching (RIE) with an inductively coupled plasma. The isolation etch of Samples C–H extended 4.5 periods into the DBR. The Ti–Au contacts were 20 μm wide. The electrical injection utilized current pulses which were 25–400 μs wide at 50% duty cycle. The optical emission was measured through a SPEX 1681B spectrometer, and collected by either an InGaAs photodetector or a photomultiplier tube.

All samples had similar layer structures, and were operated at similar current densities. The main difference between the samples was the presence or absence of a resonant cavity. Sample A was *not* placed within a resonant cavity or waveguide. A DBR was placed underneath the active layer in Samples B–H to increase the optical path for resonant normal wave vectors K_Z. In Samples A and B, Figs. 1c–d respectively show that wet-etched rough facets preclude the optical-feedback characteristic of resonant cavities. In the six Samples C–H, Fig. 1e shows that RIE facets made possible a resonant cavity and optical feedback.

3 Results

Solution of the laser rate equations [23, 24] shows three regimes of behavior. At low injection, spontaneous emission is indicated [23, 24] as a +1 slope in a log–log plot of optical emission as a function of current density J (the "L–I" curve). This indicates that the optical emission is proportional to the first power of J. At a higher injection, stimulated emission is observed, and rises much more quickly as J^s, where $s > 1$. On a log–log plot, stimulated emission shows [3, 4, 23–27] a superlinear slope s, ($s > 1$). Typical values of the superlinear slope s range from 2.5–3.5, for large microdisk lasers [25, 26] at room-temperature, to 2.9–11, for very small microdisk lasers [3, 4, 27] at low temperature. This superlinear growth of the optical emission continues until the photon number reaches $1/\beta$ [24], where β is the spontaneous emission coefficient, beyond which the laser output increases linearly with J. This linear dependence of the L–I curve at high injection indicates a pinning of the population inversion at its threshold value. At threshold, the slope of the L–I curve on a log–log plot has its greatest value [23].

Our evidence for laser action from GaAs deep centers is summarized here: (1) L–I curves, showing a superlinear regime at low injection, where the stimulated emission rises three orders of magnitude with the functional dependence J^s, and a regime linear in J at higher injection, indicating gain-pinning and laser action. The exponent s in the stimulated-emission regime is found to be larger for longer optical paths and higher quality optical confinement. (2) In the single-pass geometry of Sample B below, laser action is observed for the longest wavelength total-internal-reflection (TIR) mode of Fig. 1g. At an injection high enough for laser action in this TIR mode, the optical emission from lossy modes, such as the vertical mode of Fig. 1f, is clamped at a constant value. See Fig. 2a. (3) With a resonant cavity and RIE facets, we observed a pinning of the carrier distribution among the energy levels at all injections greater than threshold. Without a resonant cavity, previous work [5, 6] showed that an increasing injection results in a marked shift in the carrier distribution, and a rise in shorter wavelength emission. (4) With a resonant cavity and RIE facets, the dominant mode in the optical emission spectrum (Fig. 3b) is the lossy vertical mode of Fig. 1f. In order to be dominant, this lossy mode must undergo significant optical gain. A significant gain is another indicator of laser action.

Sample A was *not* placed within a resonant cavity or waveguide. Figure 1 of [5] shows that the single-pass L–I curves from Sample A rise a significant two to three orders of magnitude at every wavelength at a superlinear rate of J^3. This superlinear rise as J^3 is the signature of stimulated emission.

We found that the superlinear slope s of the stimulated emission is larger for longer optical paths. Figure 1d shows a single-pass measurement from the edge of Sample B. A bottom DBR was added in Sample B to increase the optical path for resonant normal wave vectors K_Z. Wet-etched rough facets preclude the optical-feedback characteristic of resonant cavities. Figure 1f shows the "vertical" waveguide mode, in which the longitudinal wave vector K_X is nearly zero. This vertical mode is very lossy, because 70% of the power reaching the sample surface is transmitted vertically, and lost from the waveguide. Figure 1g shows the longest wavelength total-internal-reflection (TIR) mode. Here, rays from within the semiconductor are incident upon the sample surface at the critical angle θ_C for TIR. Figure 1h shows shorter wavelength TIR modes. Here, rays from within the semiconductor are incident upon the sample surface at an angle greater than θ_C. These shorter wavelength modes make fewer passes through the active region. The vertical mode of Fig. 1f makes the largest number of passes through the active region, but is quite lossy.

Figure 2 shows L–I curves measured at room-temperature in cw mode. Figure 2a shows the single-pass L–I curves
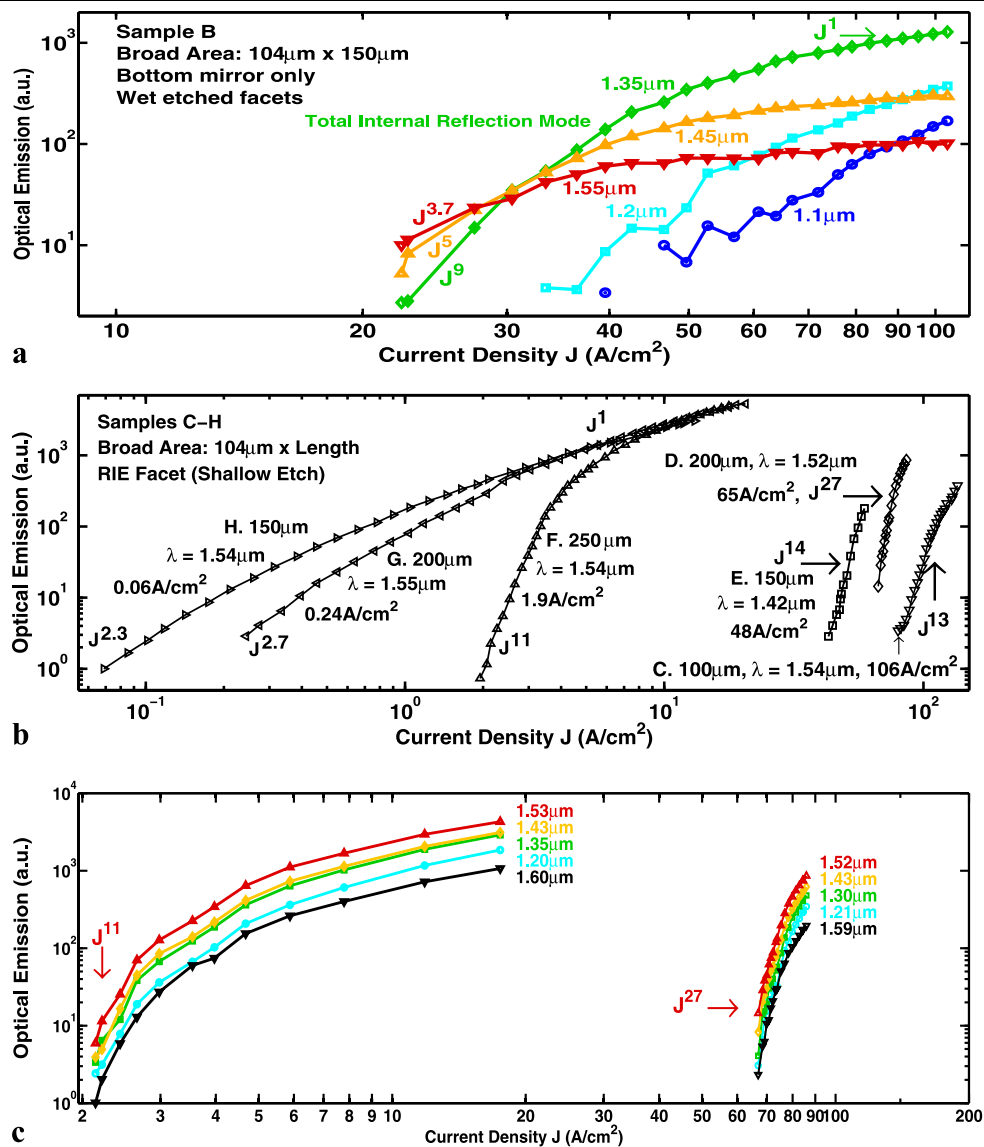
Fig. 2 (Color online) Room-temperature L–I curves measured in cw mode. **a** Single-pass optical emission from the same pixel on Sample B at different wavelengths. With an optical-path length longer than in Sample A, the stimulated emission at 1.35 μm shows a sharper rise of the optical emission as J^9. At current densities greater than 65 A/cm^2, the optical emission at 1.35 μm becomes proportional to the first power of J, and the longer wavelength (e.g., 1.45 μm and 1.55 μm) optical-emission clamps at a constant value. These two observations indicate gain pinning and single-pass laser action. **b** Optical emission at a fixed wavelength from the six different pixels C–H. Each pixel has been labeled by its length L, the measurement λ, the threshold current density (where the log–log plot of L-I shows the greatest slope), and the func-

tional form J^s of the stimulated emission. With the optical feedback resulting from RIE facets, the stimulated emission is seen to rise even more sharply as J^s, where s is as large as 27. The stimulated emission at 1.54 μm from pixel F is seen to rise a significant three orders of magnitude as J^{11}, beyond which the optical emission quickly becomes linear in J. The latter indicates gain pinning and laser action. **c** The constant vertical separation of the L–I curves at different wavelengths from the same pixel (here, pixel D and F) indicates that the optical emission has the same spectral shape for all indicated J. The latter indicates a pinning of the carrier distribution among the energy levels for all indicated J through the same pixel

from the same pixel on Sample B at different wavelengths. With the longer optical path, the stimulated emission at 1.35 μm, the longest wavelength for TIR, shows a rise as J^9 (which is a much sharper rise than from Sample A). At $J > 65$ A/cm^2, the optical emission at 1.35 μm becomes proportional to the first power of J. At these J, the longer wave-

length optical emission (e.g., at 1.45 μm for the lossy vertical mode of Fig. 1f, and also at 1.55 μm) clamps at a constant value. These two observations indicate gain pinning and single-pass laser action from Sample B. Wavelengths shorter than 1.35 μm also show stimulated emission and correspond to the modes in Fig. 1h.
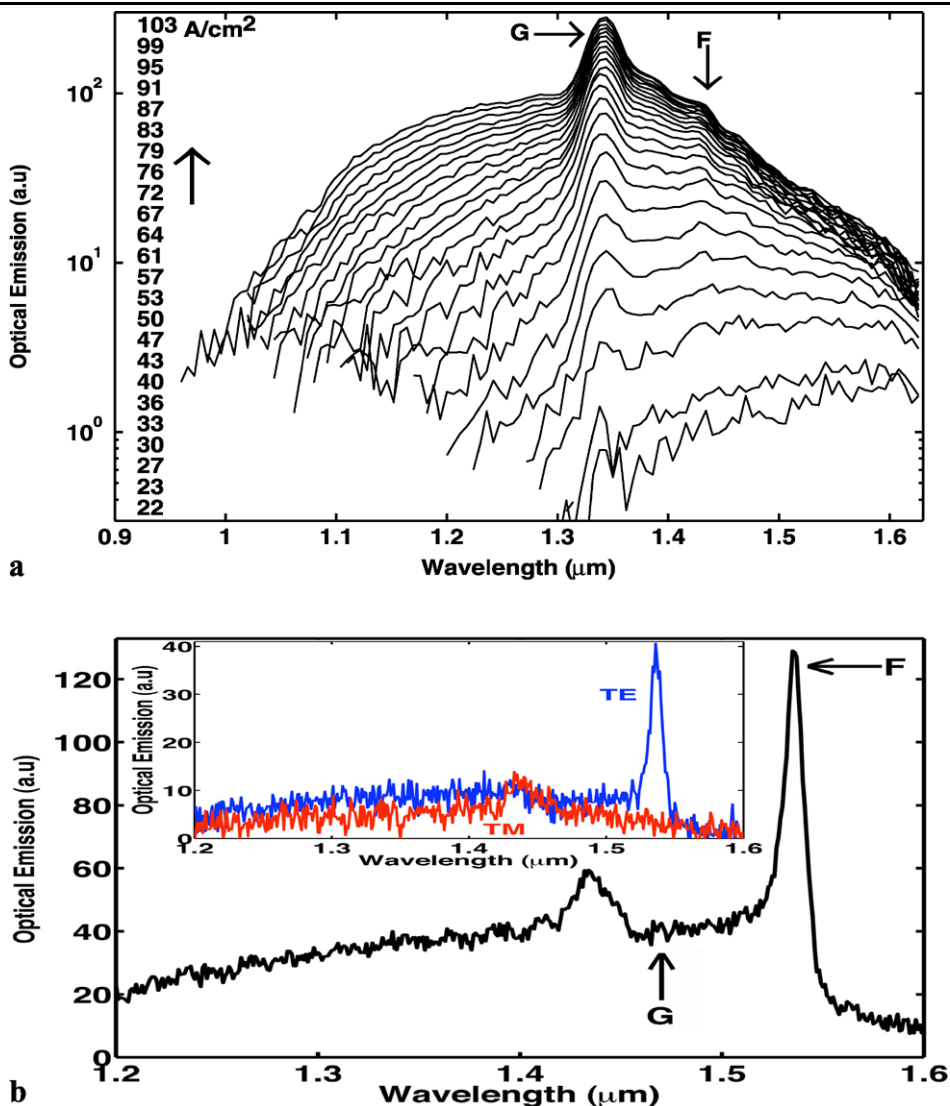
Fig. 3 (Color online) Room-temperature spectra. **a** Optical-emission spectra from Sample B. Each spectrum is labeled with the current density. After correcting for the spectrometer resolution, the width of the spectral peak was 12 nm at 103 A/cm^2. **b** Optical-emission spectra from Sample F at 17 A/cm^2. After correcting for the spectrometer resolution, the width of the spectral peak was 12 nm. (Since the vertical mode of Fig. 1f is quite lossy and has a low Q, the Fabry-Perot modes in Fig. 3b would show significant spectral overlap, and thus could not be individually resolved.) The inset shows that the peak at 1.54 μm is TE polarized. The labels F and G in Fig. 3a–b correspond to the modes shown in Fig. 1f and g, respectively. Pixels C–H all showed that the low-loss total-internal-reflection mode, labeled G in Fig. 3b, is suppressed, while the lossy vertical mode, labeled F in Fig. 3b, dominates the spectra as a narrow peak. The latter signifies that enough material gain exists to overcome the large loss incurred by the vertical mode with each trip to the sample surface. This large gain, which is needed to overcome the large loss, is another indicator of laser action. Since the vertical mode makes far more passes through the active layer than any of the total-internal-reflection modes (compare Figs. 1f, g, h), the lossy vertical mode acquires a higher net gain, and dominates Fig. 3b

In the six Samples C–H, RIE facets made possible a resonant cavity and optical feedback. See Fig. 1e. Figure 2b shows the L–I curves from the six pixels C–H. Each pixel has been labeled by its length L, the measurement wavelength λ, the threshold current density (where the log–log plot of L–I has its greatest slope), and the functional form J^s of the stimulated emission. With the optical feedback resulting from RIE facets, the stimulated emission is seen to rise even more sharply as J^s, where s is as large as 27.

The stimulated emission at 1.54 μm from pixel F is seen to rise a significant three orders of magnitude as J^{11}, beyond which the optical emission quickly becomes linear in J. The latter indicates gain pinning and laser action. Pixels F, G, H all show gain pinning by 6 A/cm^2. The threshold is less than 2 A/cm^2. Pixels C and E show an "S-shaped" L–I curve, which indicates a transition from spontaneous emission, to stimulated emission, towards laser action.

Figure 3 shows the measured room-temperature spectra. Figure 3a shows the spectra from Sample B at the indicated J. Figure 3b shows the spectra from Sample F at 17 A/cm². The inset shows that the peak at 1.54 μm is TE polarized.

We would expect that the spectral peaks in Figs. 3a–b correspond to the longest wavelength TIR mode of Fig. 1g, rather than the lossy vertical mode of Fig. 1f. (The labels F and G in Fig. 3 correspond to the modes shown in Fig. 1f and 1g, respectively.) Certainly, the single-pass measurement of Sample B in Fig. 3a indeed shows its spectral peak G at the longest wavelength TIR mode. In conventional lasers, the vertical mode of Fig. 1f never shows laser action unless *both* a top *and* bottom DBR are present. Without a top DBR, the vertical mode of Fig. 1f suffers a 70% transmission loss with every reflection at the sample surface. Thus, in the six pixels C–H, it is very significant that the lossy vertical mode dominates Fig. 3b as the narrow spectral peak F, while the low-loss TIR mode, labeled G in Fig. 3b, is suppressed. The latter signifies that enough material gain exists to overcome the large loss incurred by the vertical mode with each trip to the sample surface. This large gain, which is needed to overcome the large loss, is another indicator of laser action. Since the vertical mode makes far more passes through the active layer than any of the TIR modes (compare Figs. 1f, g, h), the lossy vertical mode acquires a higher net gain, and dominates Fig. 3b. Since the vertical mode of Fig. 1f is quite lossy and has a low Q, the Fabry-Perot modes in Fig. 3b would show significant spectral overlap, and thus could not be individually resolved.

We have observed that the lossy vertical mode of Fig. 1f ("F" in Fig. 3b) has sufficient single-pass gain to overcome the 70% transmission loss with every reflection at the sample surface. This implies that shorter wavelength TIR modes (e.g., Figs. 1g–h) also show net gain in a single-pass because TIR modes suffer *no transmission* loss at the sample surface. Gain (and laser action) is then observed over a wide wavelength range.[1] Indeed, at every wavelength between 1.2 μm and 1.6 μm, the L–I curves from pixel D (and pixel F) in Fig. 2c all show stimulated-emission regimes, followed by gain pinning and laser action. A consequence of the optical-resonator is thus to reduce the threshold at all wavelengths between 1.2 μm and 1.6 μm.

Figures. 2a, 3a, and Fig. 2 of [5] show that, in a single-pass through Samples A and B, the optical emission at shorter wavelengths increases with increasing injection.[2] This shift to shorter wavelengths of the optical emission with increasing injection was also reported in [6]. This indicates that the carrier population shifts among the energy levels with higher injection. In contrast, when an optical resonator is added, the spectra radiated by the six pixels C–H all had the same shape (shown in Fig. 3b) at all current densities measured. (This is indicated by the constant vertical separation of the curves at different wavelengths from the same pixel in Fig. 2c.) Thus, in the presence of an optical resonator, the carrier population has the *same distribution among the energy levels* for all injection currents shown in Fig. 2c (see footnote 2). This striking observation indicates that, even though the photon number is rising sharply, the carrier distribution among the energy levels is pinned. This is another indicator of laser action.

4 Conclusion

We have demonstrated the first GaAs deep-center laser. Electrically-pumped broad-area lasers exhibited a threshold of less than 2 A/cm² in cw mode at room-temperature at the 1.54 μm wavelength. In Sample B having wet-etched facets, the longest wavelength TIR mode (Fig. 1g) shows a super-linear L–I curve at low injection, and a linear regime in the L–I curve at higher injection. At injections high enough for laser action in this TIR mode, the longer wavelength optical emission is clamped at a constant value. Both observations indicate single-pass laser action and gain pinning. With a resonant cavity and RIE facets, the stimulated emission from pixel F rises a significant three orders of magnitude as J^{11} with a threshold less than 2 A/cm². With a resonant cavity and RIE facets, Pixels C–H all show a pinning of the carrier distribution among the energy levels at all injections greater than threshold. (Without a resonant cavity, previous work [5, 6] showed that an increasing injection results in a marked shift in the carrier distribution, and a rise in shorter wavelength emission.) With a resonant cavity and RIE facets, the dominant mode in the optical emission spectrum (Fig. 3b) is the lossy vertical mode of Fig. 1f. In order to be dominant, this lossy mode must undergo significant optical gain. A significant gain is another indicator of laser action.

---

[1] Inhomogeneously broadened quantum dot transitions, which show photoluminescence over a 82 nm FWHM, will then exhibit laser action over a broad 40 nm wavelength range [28–30]. The literature [28–30] shows that when the homogeneous broadening is less than the inhomogeneous broadening, the ensemble of quantum-dots acts as an array of independent lasers. In such cases, individual Fabry-Perot modes cannot be observed.

[2] The shift to shorter wavelengths of the optical emission with increasing injection was also reported in Fig. 4 of [6] for a sample fabricated without a waveguide or optical resonator. For a one decade increase in the injection, from 2 A/cm² to 20 A/cm², the optical emission from Sample A, which has no optical resonator, also shows a dramatic shift from a peak centered at 1.58 μm to a peak centered at 1.27 μm. This is shown in Fig. 2 of [5]. For a similar increase in the injection, from 2 A/cm² to 17 A/cm², the optical emission from Sample F (which does have an optical resonator) shows no change in the spectral shape. This is indicated by the constant vertical separation of the curves at different wavelengths from the same pixel in Fig. 2c.

References

1. H.G. Park, S.H. Kim, S.H. Kwon, Y.G. Ju, J.K. Yang, J.H. Baek, S.B. Kim, Y.H. Lee, Science **305**, 1444 (2004)
2. G.P. Agrawal, N.K. Dutta, *Long-Wavelength Semiconductor Lasers* (Reinhold, New York, 1986)
3. S. Reitzenstein, A. Bazhenov, A. Gorbunov, C. Hofmann, S. Muench, A. Loeffler, M. Kamp, J.P. Reithmaier, V.D. Kulakovskii, A. Forchel, Appl. Phys. Lett. **89**, 051107 (2006)
4. K.J. Luo, J.Y. Xu, H. Cao, Y. Ma, S.H. Chang, S.T. Ho, G.S. Solomon, Appl. Phys. Lett. **78**, 3397 (2001)
5. M. Gupta, J.L. Pan, J. Appl. Phys. (2009, in review)
6. J.L. Pan, J.E. McManis, M. Gupta, M.P. Young, J.M. Woodall, Appl. Phys. A **90**, 105 (2008)
7. E.W. Williams, Phys. Rev. **168**, 922 (1968)
8. H. Lei, H.S. Leipner, V. Bondarenko, J. Schreiber, J. Phys., Condens. Matter **16**, S279 (2004)
9. M. Tajima, R. Toba, N. Ishida, M. Warashina, Mater. Sci. Tech. **13**, 949 (1997)
10. M.A. Reshchikov, A.A. Gutkin, V.E. Sedov, Mater. Sci. Forum **196–201**, 237 (1995)
11. M. Suezawa, A. Kasuya, Y. Nishina, K. Sumino, J. Appl. Phys. **69**, 1618 (1991)
12. J.K. Kung, W.G. Spitzer, J. Appl. Phys. **45**, 4477 (1974)
13. S.Y. Chiang, G.L. Pearson, J. Lumin. **10**, 313 (1975)
14. T. Sauncy, C.P. Palsule, M. Holtz, S. Gangopadhyay, S. Massie, Phys. Rev. B **53**, 1900 (1996)
15. M. Suezawa, A. Kasuya, Y. Nishina, K. Sumino, J. Appl. Phys. **76**, 1164 (1994)
16. Ph. Ebert, Current Opin. Solid State Mater. Sci. **5**, 211 (2001)
17. J. Gebauer, M. Lausmann, T.E.M. Staab, R. Krause-Rehberg, M. Hakala, M.J. Puska, Phys. Rev. B **60**, 1464 (1999)
18. C. Domke, Ph. Ebert, K. Urban, Phys. Rev. B **57**, 4482 (1998)
19. C. Domke, Ph. Ebert, M. Heinrich, K. Urban, Phys. Rev. B **54**, 10288 (1996)
20. J. Gebauer, R. Krause-Rehberg, C. Domke, Ph. Ebert, K. Urban, Phys. Rev. Lett. **78**, 3334 (1997)
21. F.M. Vorobkalo, K.D. Glinchuk, A.V. Prokhorovich, G. John, Phys. Stat. Sol. (a) **15**, 287 (1973)
22. F.M. Vorobkalo, K.D. Glinchuk, A.V. Prokhorovich, Phys. Stat. Sol. (a) **7**, 135 (1971)
23. A.E. Siegman, *Lasers* (University Science Books, Mill Valley, 1986)
24. Y. Yamamoto, R.E. Slusher, Phys. Today **46**, 66 (1993)
25. N.B. Rex, R.K. Chang, L.J. Guido, IEEE Photonics Technol. Lett. **13**, 1 (2001)
26. S. Chang, N.B. Rex, R.K. Chang, G. Chong, L.J. Guido, Appl. Phys. Lett. **75**, 166 (1999)
27. S. Ates, S.M. Ulrich, P. Michler, S. Reitzenstein, A. Loeffler, A. Forchel, Appl. Phys. Lett. **90**, 161111 (2007)
28. H.S. Djie, B.S. Ooi, X.-M. Fang, Y. Wu, J.M. Fastenau, W.K. Liu, Opt. Lett. **32**, 44 (2007)
29. C.L. Tan, Y. Wang, H.S. Djie, B.S. Ooi, Appl. Phys. Lett. **91**, 061117 (2007)
30. A. Markus, J.X. Chen, C. Paranthoen, A. Fiore, C. Platz, O. Gauthier-Lafaye, Appl. Phys. Lett. **82**, 1818 (2003)